

Article

Thermocatalytic Hydrogenation of CO₂ to Methanol Using Cu-ZnO Bimetallic Catalysts Supported on Metal–Organic Frameworks

Zama G. Duma^{1,2} , Xoliswa Dyosiba¹ , John Moma^{2,*} , Henrietta W. Langmi³ , Benoit Louis⁴,
Ksenia Parkhomenko⁴  and Nicholas M. Musyoka^{1,*} 

¹ Centre for Nanostructures and Advanced Materials (CeNAM), Chemicals Cluster, Council for Scientific and Industrial Research (CSIR), Meiring Naudé Road, Brummeria, Pretoria 0184, South Africa; zduma@csir.co.za (Z.G.D.); xdyosiba@csir.co.za (X.D.)

² Molecular Sciences Institute, School of Chemistry, University of the Witwatersrand, Private Bag 2001, Johannesburg 2050, South Africa

³ Department of Chemistry, University of Pretoria, Private Bag X20, Hatfield 0028, South Africa; henrietta.langmi@up.ac.za

⁴ Energy and Fuels for a Sustainable Environment Team, Institut de Chimie et Procédés pour l’Energie, l’Environnement et la Santé, UMR 7515 CNRS—ECPM, Université de Strasbourg, 25 Rue Becquerel, CEDEX 2, 67087 Strasbourg, France; blouis@unistra.fr (B.L.); parkhomenko@unistra.fr (K.P.)

* Correspondence: john.moma@wits.ac.za (J.M.); nmusyoka@csir.co.za (N.M.M.); Tel.: +27-12-841-4806 (N.M.M.)



Citation: Duma, Z.G.; Dyosiba, X.; Moma, J.; Langmi, H.W.; Louis, B.; Parkhomenko, K.; Musyoka, N.M. Thermocatalytic Hydrogenation of CO₂ to Methanol Using Cu-ZnO Bimetallic Catalysts Supported on Metal–Organic Frameworks. *Catalysts* **2022**, *12*, 401. <https://doi.org/10.3390/catal12040401>

Academic Editors: Vincenzo Vaiano and Olga Sacco

Received: 4 March 2022

Accepted: 30 March 2022

Published: 5 April 2022

Publisher’s Note: MDPI stays neutral with regard to jurisdictional claims in published maps and institutional affiliations.



Copyright: © 2022 by the authors. Licensee MDPI, Basel, Switzerland. This article is an open access article distributed under the terms and conditions of the Creative Commons Attribution (CC BY) license (<https://creativecommons.org/licenses/by/4.0/>).

Abstract: The thermocatalytic hydrogenation of carbon dioxide (CO₂) to methanol is considered as a potential route for green hydrogen storage as well as a mean for utilizing captured CO₂, owing to the many established applications of methanol. Copper–zinc bimetallic catalysts supported on a zirconium-based UiO-66 metal–organic framework (MOF) were prepared via slurry phase impregnation and benchmarked against the promoted, co-precipitated, conventional ternary CuO/ZnO/Al₂O₃ (CZA) catalyst for the thermocatalytic hydrogenation of CO₂ to methanol. A decrease in crystallinity and specific surface area of the UiO-66 support was observed using X-ray diffraction and N₂-sorption isotherms, whereas hydrogen-temperature-programmed reduction and X-ray photoelectron spectroscopy revealed the presence of copper active sites after impregnation and thermal activation. Other characterisation techniques such as scanning electron microscopy, transmission electron microscopy, and thermogravimetric analysis were employed to assess the physicochemical properties of the resulting catalysts. The UiO-66 (Zr) MOF-supported catalyst exhibited a good CO₂ conversion of 27 and 16% selectivity towards methanol, whereas the magnesium-promoted CZA catalyst had a CO₂ conversion of 31% and methanol selectivity of 24%. The prepared catalysts performed similarly to a CZA commercial catalyst which exhibited a CO₂ conversion and methanol selectivity of 30 and 15%. The study demonstrates the prospective use of Cu-Zn bimetallic catalysts supported on MOFs for direct CO₂ hydrogenation to produce green methanol.

Keywords: CO₂ hydrogenation; bimetallic catalysts; metal–organic frameworks; catalysis; methanol economy

1. Introduction

The continuous increase in atmospheric CO₂ levels propelled by fossil fuel combustion has caused an unprecedented rise in mean global temperatures [1–4]. The increase in the atmospheric concentration of anthropogenic CO₂ contributes vastly to the greenhouse effect, which culminates in heat being trapped in the Earth’s atmosphere [5]. In recent years, there has been a collective effort to research ways to capture, store, and utilise CO₂. A possible route for curbing the deleterious effects of global warming caused by greenhouse gas emissions is the conversion of CO₂ into value-added chemicals such as methanol,

dimethyl ether, formaldehyde, and acetic acid [5–7]. The thermocatalytic hydrogenation of CO₂ is a proven approach towards the production of renewable methanol in substantial quantities [8–13]. Indeed, “The Methanol Economy” outlined by Olah et al. cites the advantages of CO₂ conversion to methanol where each molecule produced consists of four hydrogen atoms and is, therefore, a suitable energy storage molecule which is a liquid at ambient conditions. Furthermore, methanol may be used directly as a fuel in internal combustion engines to further curb the deleterious effects of anthropogenic CO₂ emissions [14]. Since the late 1960s, methanol has been produced from syngas (CO, CO₂, and H₂) over a coprecipitated ternary catalyst, Cu/ZnO/Al₂O₃, at pressures and temperatures ranging between 50 and 80 bar and 210 and 290 °C [15–17].

In recent years, Cu/ZnO/Al₂O₃ catalysts have been studied for the thermocatalytic hydrogenation of CO₂ to methanol [18–22]. Though the catalysts exhibit CO₂ conversion and methanol selectivity, the promoter effects conferred by ZnO_x, which induces morphological changes, and its function as a spacer for Cu active sites are diminished by the temperature and pressure conditions in the reactor with time [23–25]. The phase separation of Cu/ZnO_x results in the agglomeration, sintering, and poor dispersion of Cu nanoparticles, which consequently decreases activity towards methanol production due to a decrease in the metallic surface area of the Cu active sites. In addition, the deactivation attributed to the phase separation and sintering of Cu nanoparticles can catalyse the reverse water–gas shift reaction (RWGS), which produces carbon monoxide (CO) and water (H₂O) from the CO₂/H₂ inlet gas mixture, thereby decreasing the catalysts’ selectivity to methanol [23,26,27]. The phase separation of Cu-based catalysts can be circumvented by the deposition and/or encapsulation of Cu/ZnO_x nanoparticles into metal–organic frameworks (MOFs) [28,29]. MOFs are a class of highly crystalline, nanoporous materials prepared via the self-assembly of metal ion clusters and multidentate organic linkers [30,31]. Recently, MOFs have been identified as prospective supports for Cu-based CO₂ hydrogenation catalysts. Rungtaweeworanit et al., for instance, encapsulated and deposited Cu nanoparticles on a Zr-based MOF (UiO-66) and observed that the latter exhibited an 8-fold increase in turnover frequency when compared to the conventional Cu/ZnO/Al₂O₃ catalyst [4]. In addition to the confinement of Cu nanoparticles by strong support–metal interactions (SMSI), MOFs such as UiO-66 exhibit chemical promotion by charge transfer from Cu to the MOF, which significantly enhances the activity of the hybrid catalysts towards CO₂ hydrogenation [32]. Therefore, the purpose of this study is to elucidate the performance of novel Cu–Zn bimetallic catalysts supported on a zirconium-based MOF, UiO-66(Zr), prepared via slurry-phase impregnation compared with conventional ternary promoted Cu/ZnO/Al₂O₃ catalysts.

2. Results and Discussion

2.1. Characterisation

2.1.1. X-ray Diffraction and (XRD) Thermogravimetric Analysis (TGA)

The XRD analytical results of the co-precipitated commercial and CuO/ZnO/Al₂O₃/MgO catalysts are shown in Figure 1a, where the crystalline phase of CuO is observed at 35° < 2θ < 39° whilst that of ZnO can be seen at 31, 33, and 37° [5,18,33–35]. The average crystallite sizes of CuO at 2θ = 38.7° in the commercial and CuO/ZnO/Al₂O₃/MgO catalysts, calculated using the Debye–Scherrer equation, were found to be 5.2 and 7.8 nm, respectively. The smaller CuO crystallite sizes in the commercial catalyst can be attributed to a high Cu dispersion [36,37]. The XRD results of the pristine UiO-66 support and Cu/ZnO/UiO-66 also shown in Figure 1a are typical of the crystalline phase with peaks at 2θ = 7.4, 8.5 and 14.1, 14.7, 17, 18.6, and 19.1° [38,39]. Neither the copper nor zinc phases (Cu⁰, CuO, Cu₂O, or ZnO) could be observed in Cu/ZnO/UiO-66, potentially attributed to the high Cu and Zn dispersion over the framework or low metal loading [3].

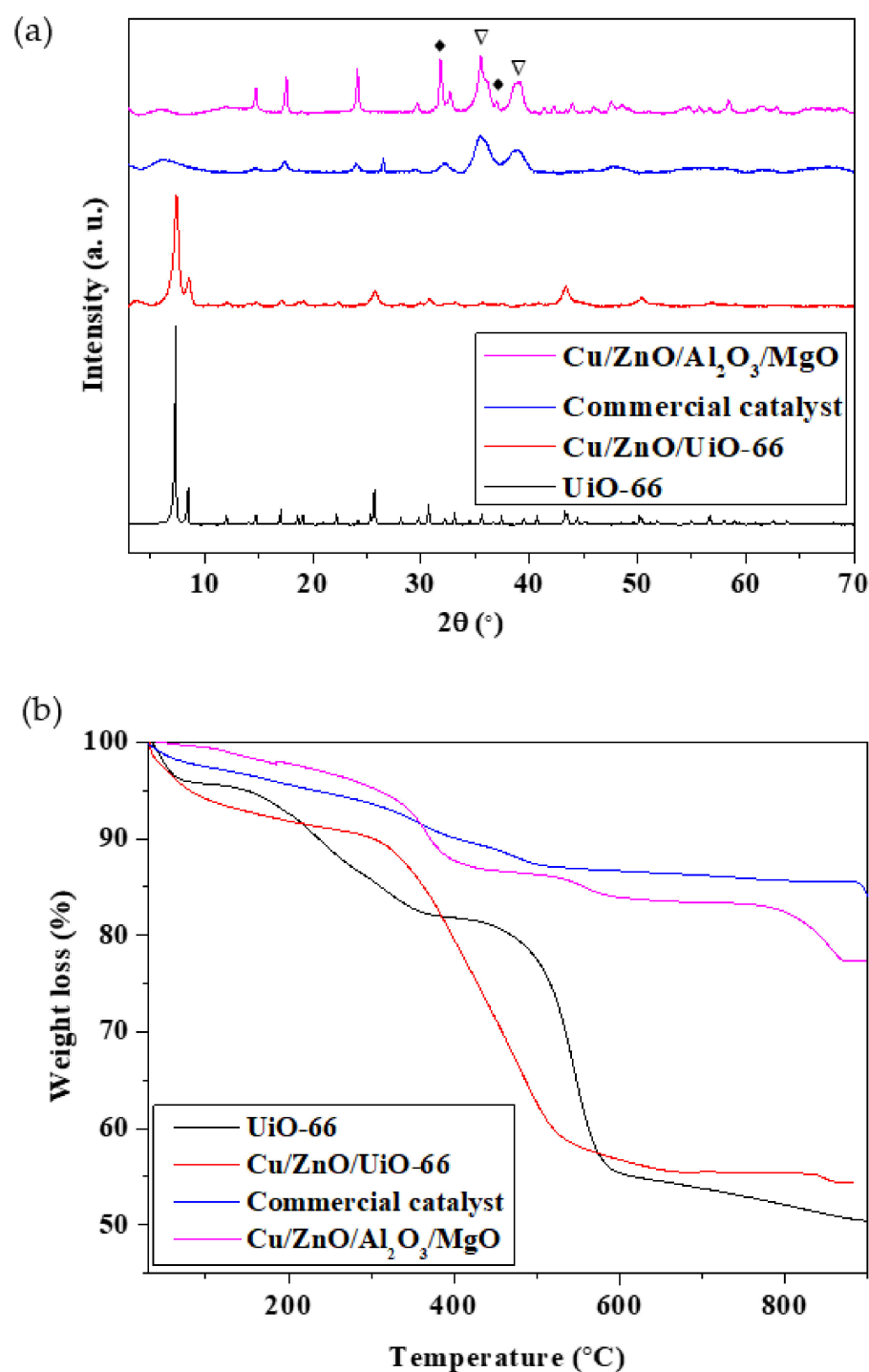


Figure 1. (a) XRD patterns and (b) TGA profiles of commercial catalyst, Cu/ZnO/Al₂O₃/MgO catalyst, UiO-66, and Cu/ZnO/UiO-66. ◆ ZnO, ▼ CuO.

The thermal stabilities of the commercial and Cu/ZnO/Al₂O₃/MgO catalysts as well as the MOF-supported catalyst were determined using thermogravimetric analysis in comparison to the commercial catalyst shown in Figure 1b. The commercial and Cu/ZnO/Al₂O₃/MgO catalysts were observed to exhibit thermal stability up to 900 $^\circ$ C. The mass loss observed in UiO-66 and Cu/ZnO/UiO-66 from 100 to 350 $^\circ$ C is attributed to the removal of dimethylformamide (DMF), ethanol, H₂O, and residual carboxylic acid groups (Figure 1b) [38,40]. The almost linear weight loss of UiO-66 and Cu/Zn/UiO-66

between 300 and 500 °C is indicative of the high thermal stability of the Zr-based MOF, after which ZrO_2 is formed due to the degradation of the organic linkers [41]. Furthermore, the thermal stability of UiO-66 decreases after impregnation and thermal activation at 350 °C. The thermal stability of the catalysts is essential for the stability under reactor conditions at 230 °C and 50 bar to prevent catalyst deactivation due to thermal degradation and MOF-support structural collapse. Therefore, all the as-prepared catalysts are anticipated to be relatively stable over time on stream while the reactor operates continuously for CO_2 hydrogenation. Furthermore, it can be seen that the commercial and Cu/ZnO/Al₂O₃/MgO catalysts are relatively more thermally stable than UiO-66 and the Cu/ZnO/UiO-66 catalyst, respectively.

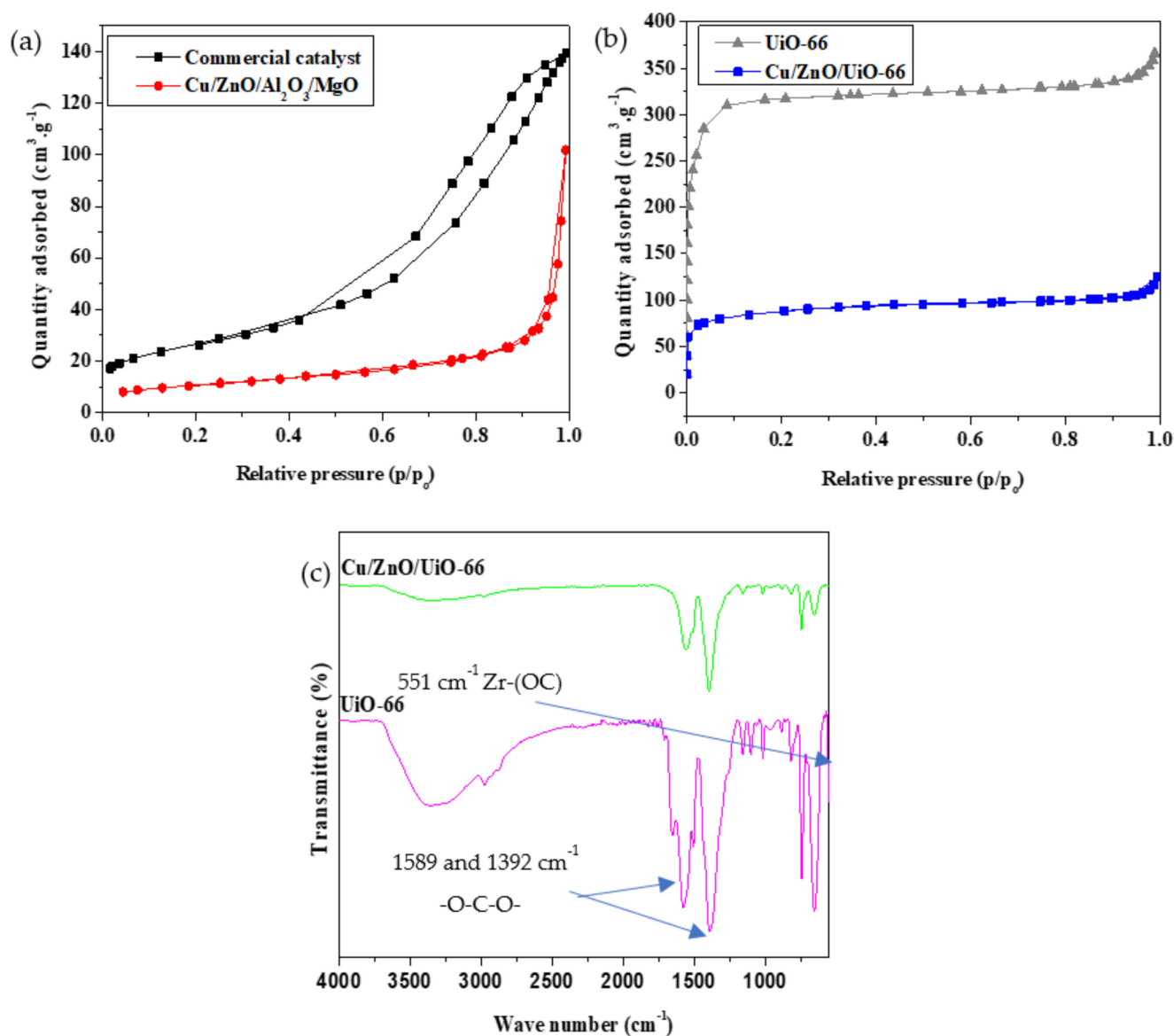
2.1.2. N₂ Physisorption, Fourier Transform Infrared Spectroscopy (FTIR), and Metal Loading

The surface area and pore volume of the catalysts and pristine UiO-66 were characterised using nitrogen adsorption–desorption isotherms where the results are listed in Table 1. The Brunauer–Emmett–Teller (BET) surface area of UiO-66 was 1238 m²/g with a pore volume of 0.47 cm³/g. The reported values are consistent with data previously reported for UiO-66 [38,40]. The nitrogen sorption isotherms of pristine UiO-66, Cu/ZnO/UiO-66, Cu/ZnO/Al₂O₃/MgO, and commercial catalysts are shown in Figure 2. It is clear from Figure 2b that both pristine and impregnated MOFs exhibit type-I sorption isotherms owing to their microporous structure. Furthermore, the decrease in specific surface area (SSA) observed in Cu/ZnO/UiO-66 can be attributed to the presence of Cu and Zn nanoparticles which occupy available surface sites of the UiO-66 support [3,32]. The commercial catalyst had a higher SSA compared to the CuO/ZnO/Al₂O₃/MgO catalyst. The effect of larger crystallite sizes, corroborated by the XRD derived data in Figure 1a, culminates in a relatively low SSA when compared to the commercial catalyst [33,42]. The functional groups of the organic linkers present in the samples were studied using FTIR (Figure 2c). The peak at 656 cm⁻¹ is attributed to the vibration of μ_3 -O in the Zr₆O₄(OH)₄(CO₂)₁₂ nodes of UiO-66, whereas the peak at 550 cm⁻¹ is due to asymmetric Zr-(OC) vibrations which further indicate successful coordination of the Zr secondary building units (SBUs) to the organic benzene dicarboxylate (BDC) linkers [3,40,43]. The stretching symmetric and asymmetric vibrations of the carboxylate group can be observed at 1572 and 1392 cm⁻¹, whereas the π C = C vibration in the aromatic benzene ring in the linker can be observed at 1508 cm⁻¹ [40,44]. The decrease in the intensity of peaks can be observed in the Cu/ZnO/UiO-66 catalyst, which may be attributed to the decrease in the amount of the functional groups, due to partial degradation, associated with UiO-66 after impregnation and thermal treatment, which is corroborated by the decrease in crystallinity and SSA seen in Figures 1a and 2b [45].

The inductively coupled plasma-optical emission spectroscopy (ICP-OES) results showed that the concentration of Cu in the Cu/ZnO/UiO-66 catalyst was 12 wt%, which confirms successful Cu impregnation although it was slightly higher than the nominal loading of 7 wt%. The amount of Zn was also found to be 4.2% compared to a loading of 3%. The discrepancy in nominal loading may be due to inhomogeneous dispersion over the UiO-66 framework, albeit scanning electron microscopy-electron dispersive X-ray spectroscopy (SEM-EDS) elemental maps revealed a good dispersion of both Cu and Zn (Figure S1). The amount of Cu, Zn, Al, and Mg in the Cu/ZnO/Al₂O₃/MgO catalysts was found to be 61.7/27.7/10.6/0.1 weight% (wt%) compared with the nominal loading of 64.2/24.5/9.8/1.3 wt%. In addition, the elemental map shows good dispersion of all the elements, and Mg was not observed in the analysis, most likely due to its low loading (Figure S2). Similarly, the EDS results of the commercial catalyst showed a good dispersion as seen in Figure S3 and a loading of 59.9, 27.5, 10.1, and 2.54 wt%, which corresponds to the certificate of analysis issued by the supplier, reporting a loading of 64.2/24.5/9.8/1.3 wt%. The elemental loading in each catalyst is summarised in Table 1.

Table 1. Specific surface area, pore volume, and elemental loading of prepared materials.

Sample	SSA (m ² /g)	Pore Volume (cm ³ /g)	Cu wt%	Zn wt%
Commercial catalyst	97	0.188	59.9	27.5
Cu/ZnO/Al ₂ O ₃ /MgO	38	0.103	61.7	27.7
UiO-66	1238	0.471	-	-
Cu/ZnO/UiO-66	561	0.200	12	4.2

**Figure 2.** Nitrogen sorption isotherms at 77 K of (a) commercial catalyst and Cu/ZnO/Al₂O₃/MgO catalyst; (b) UiO-66 and Cu/ZnO/UiO-66; and (c) FTIR spectra of UiO-66 and Cu/ZnO/UiO-66.

2.1.3. Electron Microscopies

The scanning and transmission electron microscopy (SEM and TEM) images of the samples are shown in Figure 3. The morphology of pristine UiO-66 (Figure 3a,b) is typical of octahedral-shaped crystals with a homogeneous particle size distribution [15,21,25]. The octahedral shape of UiO-66 is also preserved after impregnation with Cu and Zn (Figure 3c,d). The commercial catalyst (Figure 3e,f) exhibited irregular shapes which are typically observed when the ageing time in the mother liquor after co-precipitation is too short [46]. The CuO/ZnO/Al₂O₃/MgO catalyst (Figure 3g,h) exhibited a needle-like

morphology similar to those observed by Mota, et al., being characteristic of catalysts prepared via the zincian malachite precursor as were prepared in this study [34].

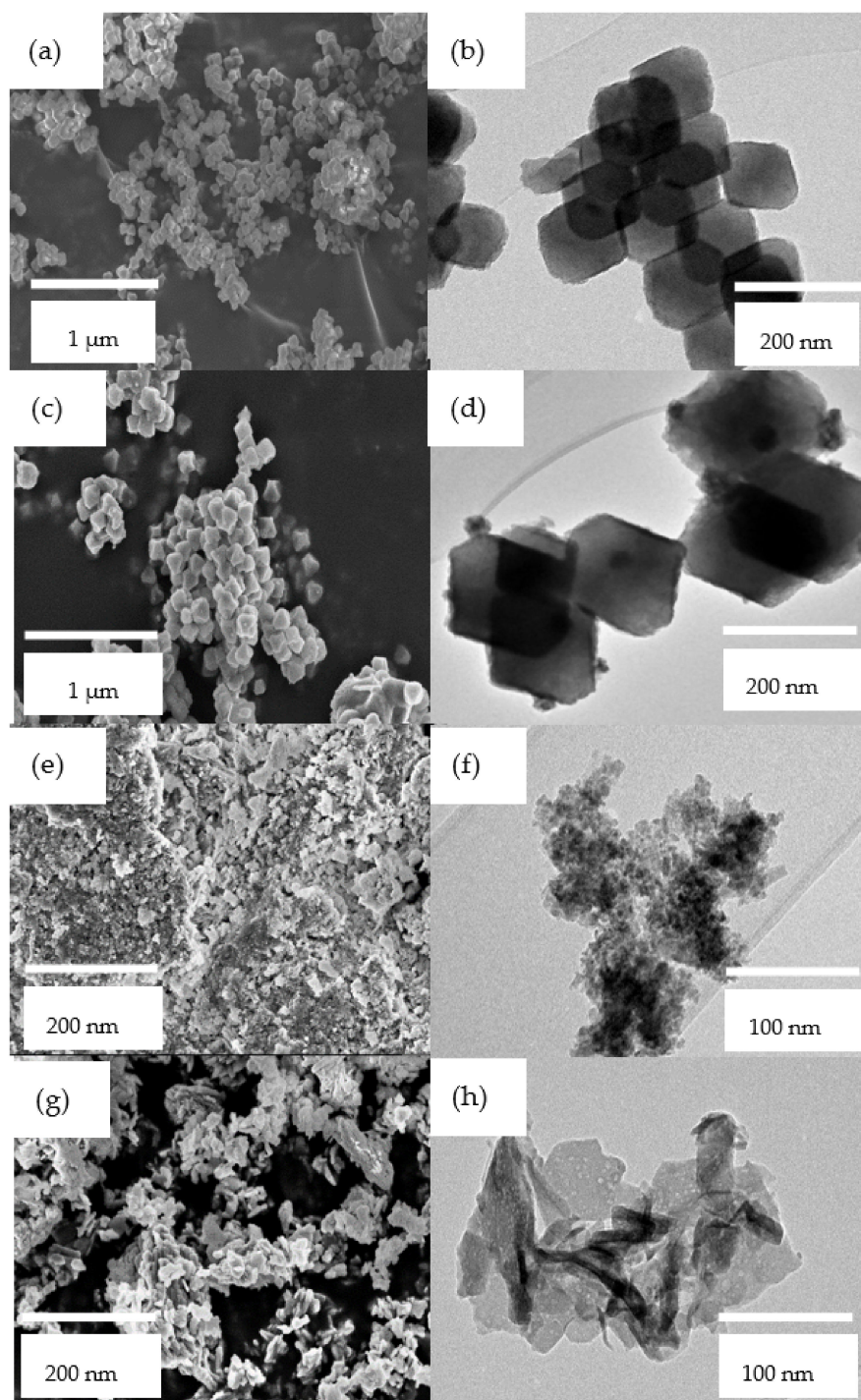


Figure 3. SEM and TEM images of (a,b) UiO-66; (c,d) Cu/ZnO/UiO-66; (e,f) commercial catalyst; and (g,h) CuO/ZnO/Al₂O₃/MgO catalyst. The images were taken at different magnifications.

The TEM images of the pristine UiO-66 and Cu/ZnO/UiO-66 catalyst shown in Figure 3b,d corroborate the octahedral shape of UiO-66 particles seen in Figure 3a,b. Furthermore, on the surface of the UiO-66 particles in the Cu/ZnO/UiO-66 catalyst, small spherical nanoparticles can be seen which are indicative of CuO/ZnO nanoparticles [4,28]. These nanoparticles are well dispersed on the surface of UiO-66 particles as indicated by

SEM-EDS (Figure S2). The micrographs confirm the successful dispersion of Cu and Zn in the Cu/ZnO/UiO-66 catalyst.

2.1.4. X-ray Photoelectron Spectroscopy (XPS)

The XPS results revealed that Cu was indeed successfully loaded on the surface of the UiO-66 support (Figure 4a,b). Cu was present as cupric hydroxide ($\text{Cu}(\text{OH})_2$) after drying at 160 °C in air. Furthermore, the $2p_{1/2}$ and $2p_{3/2}$ peaks at 934.5 and 953.6 3eV, and the satellite peak at 943 ± 0.2 eV, corroborate the presence of Cu^{2+} species (Figure 4b) [47,48]. Therefore, to ensure the preferential formation of the Cu^{2+} precursor to the copper active phase precursor, Cu^0 , the dried pre-catalyst was activated by thermal treatment under a constant flow of argon at 350 °C. CuO is desired as it is the precursor phase to the metallic Cu active phase formed by reduction with H_2 at temperatures between 200 and 300 °C [15]. Furthermore, Zr was present as ZrO_2 as revealed by the peak at Zr $3d_{5/2}$ at 182.1 eV and the Zr $3d_{3/2}$ peak at 185.2 eV, respectively (Figure 4c) [45]. XPS analysis did not detect any Zn, probably due to its low loading or high dispersion [3]. It is also likely that the analysis depth of the X-rays used in the XPS analysis are beyond the penetration depth of the Zn nanoparticles [4]. Furthermore, near ambient pressure XPS would be required to ascertain the surface and subsurface oxidation states of nanoparticles smaller than 4 nm [49]. Zn was, however, observed using SEM-EDS with a good dispersion due to the relatively high analysis depth of SEM-EDS which extends to 1–3 μM , whereas XPS is limited to up to 10 nm of the surface (Figure S1) [50,51]. The XPS results of the pristine UiO-66 support are shown in Figure S4.

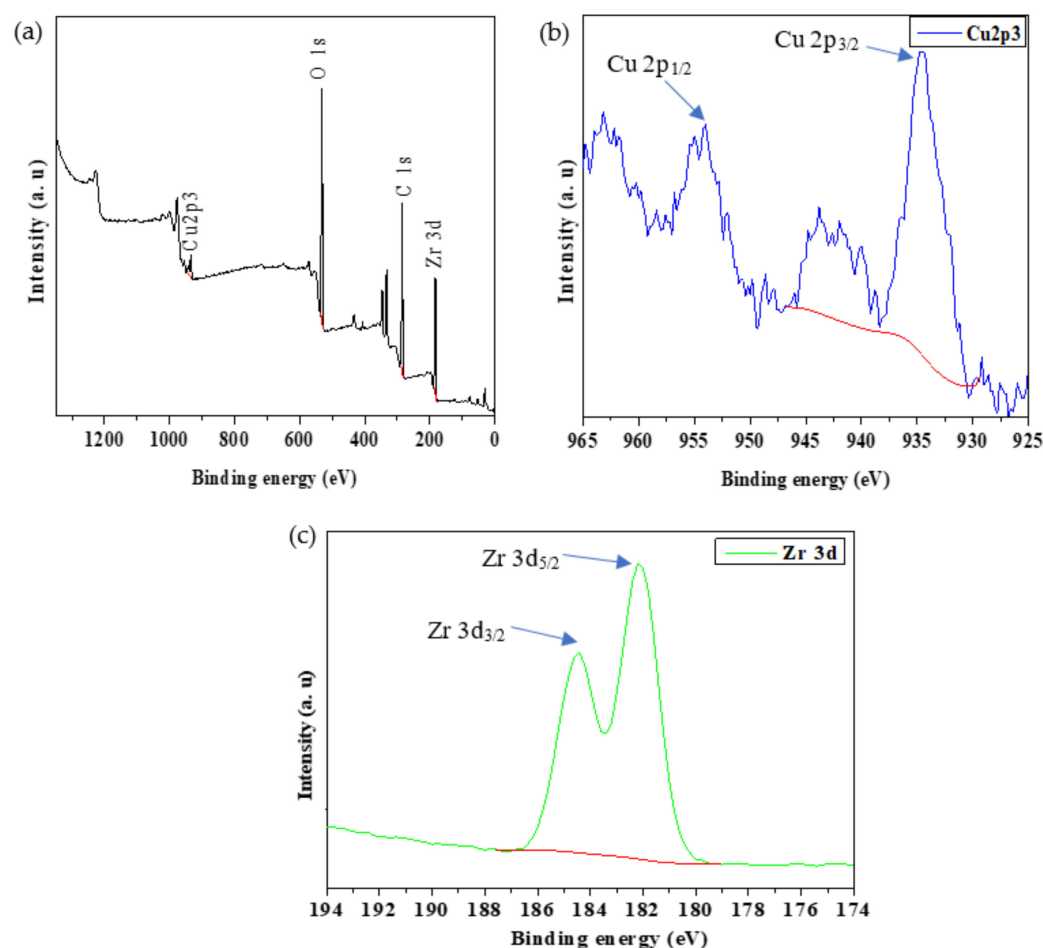


Figure 4. XPS spectra of (a) Cu/ZnO/UiO-66 full survey, (b) Cu2p3, and (c) Zr3d.

2.1.5. Hydrogen Temperature-Programmed Reduction (H₂-TPR)

The reducibility of the catalysts was studied using hydrogen temperature-programmed reduction (H₂-TPR) where the reduction profiles are shown in Figure 5. All the Cu-loaded catalysts exhibited hydrogen uptake. The commercial and Cu/ZnO/Al₂O₃/MgO catalysts showed reduction peaks at $T_{max} = 195$ °C and 223 °C (Figure 5a). The reduction peaks are indicative of CuO crystallite formed after calcination. The broader curve of the Cu/ZnO/Al₂O₃/MgO may be due to the larger CuO crystallite size of 7.8 nm compared to 5.2 nm in the commercial catalyst [5,34]. The H₂-TPR profiles of UiO-66 and Cu/ZnO/UiO-66 are in Figure 5b, where no Cu reduction peak was seen for pristine UiO-66. H₂ uptake, conversely, was observed in Cu/ZnO/UiO-66 at $T_{max} = 209$ °C; the reduction peak further corroborates the presence of H₂-active copper species on the surface of UiO-66 [45]. The peaks at $T_{max} = 446$ °C in Figure 5b indicate the reduction of Zr species in the metal centre or clusters of the UiO-66 framework. It can also be seen that the loading of Cu and Zn on UiO-66 shifts the T_{max} of the ZrO₂ reduction peak to 446 °C, which may be due to the ease of reduction facilitated by H₂ spillover from Cu and Zn, respectively [45,52].

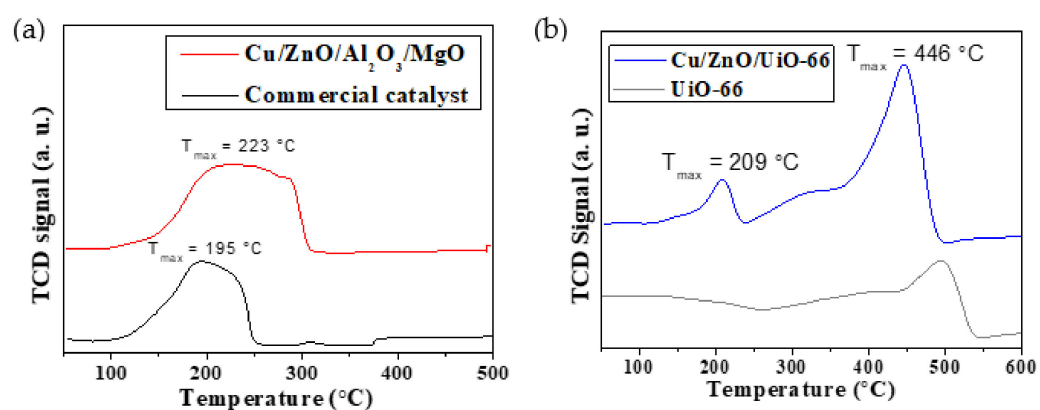
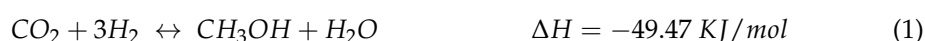


Figure 5. H₂-TPR profiles of the prepared catalysts: (a) Commercial and Cu/ZnO/Al₂O₃/MgO catalysts; (b) UiO-66 and Cu/ZnO/UiO-66.

2.2. Catalyst Testing and Evaluation

Conversion, Selectivity and Productivity

The CO₂ conversion results of all catalysts are shown in Figure 6. In the study, it was predominantly CO, MeOH, and methane (CH₄) that were formed as products in addition to H₂O. The reaction progresses through the exothermic CO₂ hydrogenation reaction shown in Equation (1). CO is formed via the endothermic reverse water–gas shift reaction in which CO₂ is reduced to CO and H₂O, Equation (2) [4,10,15,26]. In addition, CH₄ was presumably formed via the Sabatier reaction, in which CO₂ methanation takes place to form CH₄ and H₂O, Equation (3) [53]. The highest average CO₂ conversion after 24 h online was exhibited by the Cu/ZnO/Al₂O₃/MgO catalyst (30.6%) followed by the commercial catalyst (29.8%) and the Cu/ZnO/UiO-66 catalyst (26.7%). Furthermore, all the catalysts tested exhibited a good stability within the 24 h evaluation period.



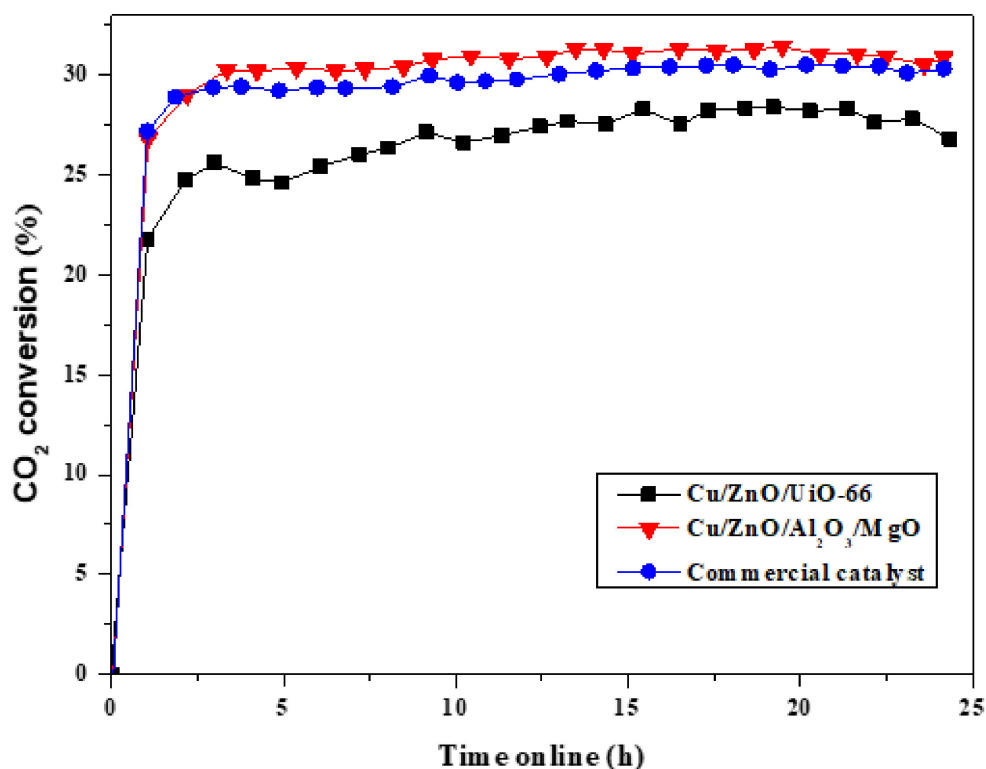


Figure 6. CO₂ conversions of catalysts. T = 230 °C; P = 50 bar; Q_{v,0} = 40 mL·min⁻¹; GHSV = 10,000 h⁻¹.

The selectivity of the catalysts towards methanol was also evaluated, where the Cu/ZnO/Al₂O₃/MgO catalyst exhibited the highest selectivity towards methanol (24%) followed by the Cu/ZnO/UiO-66 catalyst (16%), whereas the commercial catalyst had the lowest selectivity of 15.0% (Figure 7a). Furthermore, owing to the competing RWGS in thermocatalytic CO₂ hydrogenation, the selectivity of the catalysts towards CO was evaluated [54]. As can be seen in Figure 7b, the selectivity of the catalysts towards CO was very high for all catalysts with the highest, at 84%, exhibited by the commercial catalyst, despite small CuO crystallites and a high SSA, which are anticipated to suppress CO selectivity [23,26]. In contrast, the Cu/ZnO/Al₂O₃/MgO and Cu/ZnO/UiO-66 catalysts had relatively lower CO selectivities of 74 and 83%, respectively. In addition, CH₄ was also observed in the product streams of all the catalysts, which is presumably from the Sabatier reaction in which CO₂ methanation occurs [53]. As such, the Cu/ZnO/UiO-66 and Cu/ZnO/Al₂O₃/MgO catalysts had the most selectivity towards CH₄ at 1.6 and 1.7%, respectively, with the lowest observed in the commercial catalyst (0.9%). The methanol productivity, space-time yield (STY), of the Cu/ZnO/UiO-66 catalyst commercial catalyst was 128 g_{MeOH}/Kg_{cat}/h, followed by the commercial catalyst at 52 g_{MeOH}/Kg_{cat}/h (Figure 7d). The Cu/ZnO/Al₂O₃/MgO catalyst had the lowest methanol productivity at 37 g_{MeOH}/Kg_{cat}/h, which may be attributed to the relatively large CuO crystallite size and consequently low SSA [54].

In comparison to An et al., who observed a 100% methanol selectivity, the Cu/ZnO/UiO-66 catalyst showed a relatively low methanol selectivity of 15.7%. However, they also reported relatively low CO₂ conversions of 3.3% at a GHSV of 18,000 h⁻¹ compared to 10,000 h⁻¹, as high GHSV results in low per-pass conversion [55]. Furthermore, the commercial and Cu/ZnO/Al₂O₃/MgO co-precipitated catalysts also exhibit superior CO₂ conversion when compared to the 11% observed by Portha et al., although their catalyst, with a copper-zinc-alumina composition, exhibited a methanol selectivity of 43% compared to the 24% of the Cu/ZnO/Al₂O₃/MgO catalyst in this work [56]. These results highlight the promise of using Cu-based MOF-supported catalysts for CO₂ hydrogenation to methanol due to the relatively good catalytic performance of Cu/ZnO/UiO-66 despite

having ten times less the Cu loading compared to the Cu/ZnO/Al₂O₃/MgO and commercial catalysts. The high CO₂ conversion and relative methanol STY may be attributed to the good dispersion of Cu over UiO-66, the high SSA, and the enhancement of the active sites by the ZrO₂ secondary building units [4,57].

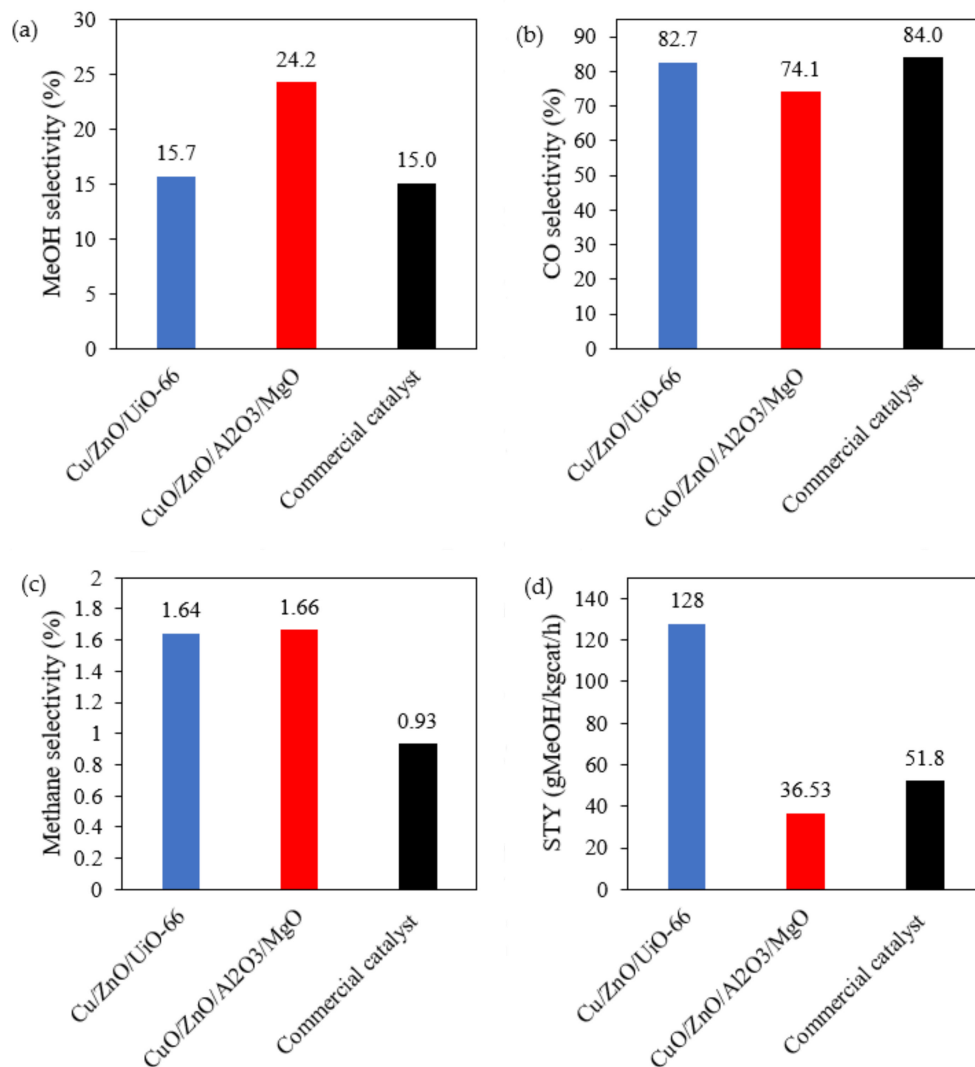


Figure 7. Catalysts' (a) methanol selectivity; (b) CO selectivity; (c) methane selectivity and (d) space-time yield.

3. Materials and Methods

3.1. Reagents and Chemicals

Ethanol (Associated Chemical Enterprises, 95%), *N,N*-dimethyl formamide (Associated Chemical Enterprises, 99.5%), cupric nitrate trihydrate (Cu(NO₃)₃·3H₂O, Associated Chemical Enterprises, 99.9%), magnesium nitrate hexahydrate (Mg(NO₃)₂·6H₂O, Associated Chemical Enterprises, 98%), zinc nitrate hexahydrate (Zn(NO₃)₂·6H₂O, Associated Chemical Enterprises, 99.9%), zirconium tetrachloride (ZrCl₄, Sigma-Aldrich, 99.5%), terephthalic acid (Sigma-Aldrich, 98%), and aluminium nitrate nonahydrate (Al(NO₃)₃·9H₂O, Sigma-Aldrich, ≥98%) were commercially sourced from Associated Chemical Enterprises Pty Ltd. (Johannesburg, South Africa) and Merck KGaA (Darmstadt, Germany), and used without further purification. De-ionised water was sourced from a water demineralisation system (Instrubal, Zener Power II) located on-site. A copper-based methanol synthesis catalyst was procured from Alfa Aesar, Thermo Fischer Scientific (Kandel, Germany). The

pelletised catalyst with a percentage composition of 64.2/24.5/9.8/1.3 (Cu/Zn/Al/Mg) was ground to a powder with a pestle and mortar before any use.

3.2. Catalysts' Synthesis

3.2.1. Cu/ZnO/Al₂O₃/MgO Catalyst

The Cu/ZnO/Al₂O₃/MgO catalyst was prepared via a co-precipitation method. In the procedure, a catalyst with a mass percentage loading of 64.2/24.5/9.8/1.3 (Cu/Zn/Al/Mg) was prepared by dissolving 50.5 mmol of Cu(NO₃)₂·3H₂O, 11.9 mmol of Zn(NO₃)₂·6H₂O, 10.3 mmol of Al(NO₃)₃·9H₂O, and 1.55 mmol of Mg(NO₃)₂·6H₂O in demineralised water (90 mL) followed by acidification with 20 mL of 65% HNO₃ to give a 1 M metal nitrates' solution. The solution, maintained at 60 °C, was dosed with 1 M Na₂CO₃ solution at a rate of 3 mL/min whilst stirring at 400 rpm. Once the solution reached a pH of 6.5 ± 0.5, it was left to age for 1 h. The solution was then filtered, and the precipitates were washed several times with demineralised water and then dried overnight at 90 °C. The dried precursors were then calcined in open air at 330 °C for 3 h.

3.2.2. UiO-66 (Zr) MOF Synthesis

UiO-66 MOFs were prepared via a modified solvothermal method reported by Ren et al. (2014) [38]. In the procedure, terephthalic acid (4.54 mmol) and ZrCl₄ (4.54 mmol) were dissolved in 500 mL of dimethylformamide (DMF) and dissolved by magnetic stirring in a beaker at room temperature. After dissolution, 171.3 mL of formic acid (0.453 mmol) was added as a modulator. The crystallisation of UiO-66 was carried out at a constant reaction temperature of 120 °C under static reflux for 4 h. The white precipitate was recovered by vacuum filtration, washed by immersing in a round-bottom flask with hot ethanol at 60 °C overnight, vacuum filtered, and dried at 90 °C for 24 h.

3.2.3. UiO-66 (Zr) MOF-Supported Catalyst Synthesis

Cu((NO₃)₂·3H₂O (9.97 mmol) and Zn(NO₃)₂·6H₂O (4.06 mmol) were dissolved in 14 mL of ethanol. Thereafter, UiO-66 (8.005 g) was added slowly to the metal nitrate ethanolic solution with continuous stirring. The mixture was then dried overnight at ambient temperature. The dried, light blue, catalyst precursor was thermally treated at 350 °C for 4 h under a constant flow of argon and a heating rate of 5 °C/min to furnish a 7/3/90 wt% Cu/ZnO/UiO-66 catalyst.

3.3. Characterisation

Powder X-ray diffraction (PXRD), for phase identification, was conducted with a Rigaku Ultima IV diffractometer with a Ni-filtered radiation of 0.154 nm, a voltage of 40 kV, and a current of 30 mA at room temperature (Akishima-shi, Tokyo, Japan). A scanning range of 2θ = 3–90° at a rate of 0.01° s⁻¹ was used for all the samples.

The thermal stability of the precursors and catalysts was measured using thermogravimetric analysis (TGA) using the Mettler, Toledo TGA/SDTA 851^e instrument (Mettler Toledo, Greifensee, Switzerland). In the procedure, 10 mg of the sample was heated to 1000 °C at a rate of 10 °C min⁻¹ in nitrogen.

Surface area and porosity measurements were performed with an ASAP 2020 HD analyser (Micromeritics Instrument Corporation, Georgia, United States of America), and high purity (99.999%) grade nitrogen (N₂) gas. The Brunauer–Emmett–Teller (BET) surface area and pore volume were determined using N₂ gas sorption isotherms at 77 K and relative partial pressures (*p/p*₀) of up to 1. Prior to each analysis, the samples (>0.2 g) were degassed under vacuum using a Micromeritics SmartVac with heating to no more than 200 °C.

Fourier transform infrared spectroscopy (FTIR) was recorded on a PerkinElmer Spectrum 100 FTIR spectrometer at a mid-IR range of 4000–550 cm⁻¹ (PerkinElmer, Waltham, United States of America).

The powder skeletal density of the samples was determined using a Micromeritics AccuPyc II 1340 pycnometer and helium gas at 135 kPa (Micromeritics Instrument Corporation, Georgia, United States of America).

The morphology of the samples was imaged using an Auriga Cobra focused-ion beam scanning electron microscope coupled with energy-dispersive X-ray spectroscopy (Zeiss, Oberkochen, Germany). Prior to imaging and elemental mapping, the samples were mounted on an adhesive carbon tape loaded on a sample holder and coated with carbon to prevent charging. An FEI Tecnai T12 transmission electron microscope (Thermo Fischer Scientific, Kandel, Germany) was used to image the Cu/ZnO/UiO-66 catalyst. The sample was crushed to a fine powder, dispersed in ethanol by ultrasonication, and a drop was placed on a carbon-coated copper grid which was loaded into the microscope. Elemental analyses were done using EDS for the commercial and Cu/ZnO/Al₂O₃/MgO catalysts, whereas inductively coupled plasma-optical emission spectroscopy was used for the MOF-supported catalyst. The latter was digested in aqua regia using a microwave, the digest made up to 50 mL with deionised water and analysed using ICP-OES PlasmaQuant 9100 (Analytik Jena GmbH, Jena, Germany).

Temperature-programmed reduction was used for reducibility testing using a Micromeritics Autochem II analyser (Micromeritics Instrument Corporation, Georgia, United States of America). Each sample, placed between two pieces of glass wool in a U-tube, was degassed at 150 °C at a heating rate of 10 °C/min under a constant flow of helium for 30 min and then cooled to 50 °C. Thereafter, the sample was heated to 900 °C at 10 °C/min under a 50 mL/min flow of 5% H₂/Ar. The hydrogen consumption was measured using a thermal conductivity detector.

The surface oxidation state of Cu, chemical composition of the SBUs, and metal oxide bonds were characterised using X-ray photoelectron spectroscopy (XPS). A Thermo Scientific ESCALAB 250Xi instrument was used with a monochromatic X-ray Al source with an energy of 1486.7 eV, which was operated at 300 W and a pass energy of 100 eV. The analysis was conducted under an ultrahigh vacuum of <10⁻⁸ mbar (Thermo Fischer Scientific, Kandel, Germany).

3.4. Catalyst Testing

Synthesised catalysts were tested in a fixed-bed reactor. The reactor was 21 cm in length with an internal and external diameter of 1.01 cm and 1.27 cm. Typically, the catalyst was sieved to a 50–125 µm size fraction, weighed and packed between two pieces of inert glass wool, and positioned at the centre of the reactor. Before each run, the catalyst was reduced under a stream of pure hydrogen for approximately 2 h at 40 mL/min, 250 °C, and 20 bar. Thereafter, the reactor was cooled to 50 °C, and a pre-mixed gas consisting of 3:1:0.2 H₂/CO₂/Ar was introduced into the reactor and left for 12 h to stabilise. A CO₂ hydrogenation reaction was then carried out at 230 °C, 50 bar, and a flow rate of 40 mL/min with a constant GHSV of 10,000 h⁻¹ for 24 h. The analysis of the outgoing products was carried out using an Agilent 7890B gas chromatograph instrument (Agilent Technologies Inc, California, United States of America) equipped with an FID (CH₃OH, CH₄) and two TCDs (Ar, CO, CO₂, CH₄, and H₂). Online analysis was carried out for all the outlet gases, whereas the liquid products were condensed in a trap maintained at 0 °C and injected into the GC. The conversions of CO₂ were calculated according to Equation (4).

$$X_{\text{CO}_2} = 1 - \left[\left(\frac{\text{CO}_{2, \text{out}}}{\text{CO}_{2, \text{in}}} \right) \times \left(\frac{Ar_{\text{in}}}{Ar_{\text{out}}} \right) \right] \quad (4)$$

The selectivity for methanol, CO, and CH₄ were calculated using Equations (5)–(7):

$$S_{\text{CH}_3\text{OH}} = \frac{n_{\text{CH}_3\text{OH}}}{n_{\text{CH}_3\text{OH}} + n_{\text{CH}_4} + n_{\text{CO}}} \quad (5)$$

$$S_{\text{CO}} = \frac{n_{\text{CO}}}{n_{\text{CH}_3\text{OH}} + n_{\text{CH}_4} + n_{\text{CO}}} \quad (6)$$

$$S_{CH_4} = 1 - (S_{CO} + S_{CH_3OH}) \quad (7)$$

4. Conclusions

In this study, a Zr-based MOF, UiO-66, was used as a support to prepare catalysts via slurry phase impregnation with Cu as well as Zn and tested for the thermocatalytic conversion of CO₂ to methanol. The catalyst was benchmarked against the conventional, co-precipitated, MgO-promoted ternary catalyst, and a CZA commercial catalyst. Hydrogen uptake shown by TPR revealed the presence of active Cu species for H₂ uptake and a good dispersion of Cu and Zn over the UiO-66 support was observed from SEM-EDS elemental maps. Furthermore, the performance of Cu/ZnO/UiO-66 displayed a good CO₂ conversion, selectivity towards methanol, and the highest methanol space–time yield, making MOF-supported Cu-based catalysts promising for their utilisation in the thermocatalytic hydrogenation of CO₂ to methanol.

Supplementary Materials: The following supporting information can be downloaded at <https://www.mdpi.com/article/10.3390/catal12040401/s1>, Figure S1: Elemental maps of Cu/ZnO/UiO-66; Figure S2: Elemental maps of Cu/ZnO/Al₂O₃/MgO catalyst; Figure S3: Elemental maps of commercial catalyst; Figure S4: XPS results of UiO-66: (a) full survey, (b) Zr3d, and O1s scans.

Author Contributions: Conceptualization, Z.G.D., B.L., K.P., and N.M.M.; methodology, Z.G.D., B.L., and K.P.; investigation, Z.G.D.; resources, N.M.M., H.W.L., and J.M.; writing—original draft preparation, Z.G.D.; writing—review and editing, Z.G.D., H.W.L., J.M., N.M.M., X.D., and B.L.; supervision, N.M.M., H.W.L., and J.M.; formal analysis, X.D.; funding acquisition, N.M.M., B.L., and H.W.L. All authors have read and agreed to the published version of the manuscript.

Funding: This research was funded by Royal Society Foreign, Commonwealth & Development Office (FCDO) Africa Capacity Building Initiative (ACBI) Programme (grant AQ150029) and the South African Department of Science and Innovation (DSI) for research activities under HySA Infrastructure (grant No. CNMH20X).

Acknowledgments: The authors would like to acknowledge financial support from the Royal Society Foreign, Commonwealth & Development Office (FCDO) Africa Capacity Building Initiative (ACBI) Programme (grant AQ150029), the Council for Scientific and Industrial Research (CSIR), and the South African Department of Science and Innovation (DSI) for research activities under HySA Infrastructure (grant No. CNMH20X) and the South Africa–France PROTEA Programme, which is a bilateral incentive programme dedicated to strengthening research collaborations between the two countries (project No. CNMH02X).

Conflicts of Interest: The authors declare no personal or financial conflict of interest.

References

1. Tursunov, O.; Kustov, L.; Kustov, A. A Brief Review of Carbon Dioxide Hydrogenation to Methanol Over Copper and Iron Based Catalysts. *Oil Gas Sci. Technol. Rev. IFP Energ. Nouv.* **2017**, *72*, 30. [[CrossRef](#)]
2. Fischer, H.; Wahlen, M.; Smith, J.; Mastroianni, D.; Deck, B. Ice core records of atmospheric CO₂ around the last three glacial terminations. *Science* **1999**, *283*, 1712–1714. [[CrossRef](#)] [[PubMed](#)]
3. Stawowy, M.; Ciesielski, R.; Maniecki, T.; Matus, K.; Łuźny, R.; Trawczynski, J.; Silvestre-Albero, J.; Łamacz, A. CO₂ Hydrogenation to Methanol over Ce and Zr Containing UiO-66 and Cu/UiO-66. *Catalysts* **2020**, *10*, 39. [[CrossRef](#)]
4. Rungtaweivoranit, B.; Baek, J.; Araujo, J.R.; Archanjo, B.S.; Choi, K.M.; Yaghi, O.M.; Somorjai, G.A. Copper Nanocrystals Encapsulated in Zr-based Metal–Organic Frameworks for Highly Selective CO₂ Hydrogenation to Methanol. *Nano Lett.* **2016**, *16*, 7645–7649. [[CrossRef](#)] [[PubMed](#)]
5. Gesmanee, S.; Koo-Amornpattana, W. Catalytic hydrogenation of CO₂ for methanol production in fixed-bed reactor using Cu-Zn supported on gamma-Al₂O₃. *Energy Procedia* **2017**, *138*, 739–744. [[CrossRef](#)]
6. Bowker, M. Methanol Synthesis from CO₂ Hydrogenation. *ChemCatChem* **2019**, *11*, 4238–4246. [[CrossRef](#)]
7. Fichtl, M.B.; Schlereth, D.; Jacobsen, N.; Kasatkin, I.; Schumann, J.; Behrens, M.; Schlögl, R.; Hinrichsen, O. Kinetics of deactivation on Cu/ZnO/Al₂O₃ methanol synthesis catalysts. *Appl. Catal. A Gen.* **2015**, *502*, 262–270. [[CrossRef](#)]
8. Markewitz, P.; Kuckshinrichs, W.; Leitner, W.; Linssen, J.; Zapp, P.; Bongartz, R.; Schreiber, A.; Müller, T.E. Worldwide innovations in the development of carbon capture technologies and the utilization of CO₂. *Energy Environ. Sci.* **2012**, *5*, 7281–7305. [[CrossRef](#)]
9. Wang, W.; Wang, S.; Ma, X.; Gong, J. Recent advances in catalytic hydrogenation of carbon dioxide. *Chem. Soc. Rev.* **2011**, *40*, 3703–3727. [[CrossRef](#)]

10. Shi, Z.; Tan, Q.; Tian, C.; Pan, Y.; Sun, X.; Zhang, J.; Wu, D. CO₂ hydrogenation to methanol over Cu-In intermetallic catalysts: Effect of reduction temperature. *J. Catal.* **2019**, *379*, 78–89. [[CrossRef](#)]
11. Centi, G.; Perathoner, S.; Rak, Z.S. Reduction of greenhouse gas emissions by catalytic processes. *Appl. Catal. B Environ.* **2003**, *41*, 143–155. [[CrossRef](#)]
12. Song, C. Global challenges and strategies for control, conversion and utilization of CO₂ for sustainable development involving energy, catalysis, adsorption and chemical processing. *Catal. Today* **2006**, *115*, 2–32. [[CrossRef](#)]
13. Dorner, R.W.; Hardy, D.R.; Williams, F.W.; Willauer, H.D. Heterogeneous catalytic CO₂ conversion to value-added hydrocarbons. *Energy Environ. Sci.* **2010**, *3*, 884–890. [[CrossRef](#)]
14. Olah, G.A.; Goepfert, A.; Prakash, G.S. *Beyond Oil and Gas: The Methanol Economy*. John Wiley & Sons: Hoboken, NJ, USA, 2018.
15. Natesakhawat, S.; Lekse, J.W.; Baltrus, J.P.; Ohodnicki, P.R.; Howard, B.H.; Deng, X.; Matranga, C. Active Sites and Structure–Activity Relationships of Copper-Based Catalysts for Carbon Dioxide Hydrogenation to Methanol. *ACS Catal.* **2012**, *2*, 1667–1676. [[CrossRef](#)]
16. Agarwal, A.S.; Rode, E.; Sridhar, N.; Hill, D. Conversion of CO₂ to Value-Added Chemicals: Opportunities and Challenges. In *Handbook of Climate Change Mitigation and Adaptation*; Chen, W.-Y., Suzuki, T., Lackner, M., Eds.; Springer: New York, NY, USA, 2014; pp. 1–40.
17. Etim, U.J.; Song, Y.; Zhong, Z. Improving the Cu/ZnO-Based Catalysts for Carbon Dioxide Hydrogenation to Methanol, and the Use of Methanol As a Renewable Energy Storage Media. *Front. Earth Sci.* **2020**, *8*. [[CrossRef](#)]
18. Ahouari, H.; Soualah, A.; Le Valant, A.; Pinard, L.; Magnoux, P.; Pouilloux, Y. Methanol synthesis from CO₂ hydrogenation over copper based catalysts. *React. Kinet. Mech. Catal.* **2013**, *110*, 131–145. [[CrossRef](#)]
19. Qaderi, J. A brief review on the reaction mechanisms of CO₂ hydrogenation into methanol. *Int. J. Innov. Res. Sci. Stud.* **2020**, *3*, 53–63. [[CrossRef](#)]
20. Melián-Cabrera, I.; López Granados, M.; Fierro, J.L.G. Reverse Topotactic Transformation of a Cu–Zn–Al Catalyst during Wet Pd Impregnation: Relevance for the Performance in Methanol Synthesis from CO₂/H₂ Mixtures. *J. Catal.* **2002**, *210*, 273–284. [[CrossRef](#)]
21. Wang, J.; Funk, S.; Burghaus, U. Indications for Metal-support Interactions: The Case of CO₂ Adsorption on Cu/ZnO(0001). *Catal. Lett.* **2005**, *103*, 219–223. [[CrossRef](#)]
22. Waugh, K.C. Methanol Synthesis. *Catal. Today* **1992**, *15*, 51–75. [[CrossRef](#)]
23. Kuld, S.; Thorhauge, M.; Falsig, H.; Elkjær, C.F.; Helveg, S.; Chorkendorff, I.; Sehested, J. Quantifying the promotion of Cu catalysts by ZnO for methanol synthesis. *Science* **2016**, *352*, 969–974. [[CrossRef](#)] [[PubMed](#)]
24. Spencer, M.S. The role of zinc oxide in Cu/ZnO catalysts for methanol synthesis and the water–gas shift reaction. *Top. Catal.* **1999**, *8*, 259. [[CrossRef](#)]
25. Prieto, G.; Meeldijk, J.D.; de Jong, K.P.; de Jongh, P.E. Interplay between pore size and nanoparticle spatial distribution: Consequences for the stability of CuZn/SiO₂ methanol synthesis catalysts. *J. Catal.* **2013**, *303*, 31–40. [[CrossRef](#)]
26. An, X.; Li, J.; Zuo, Y.; Zhang, Q.; Wang, D.; Wang, J. A Cu/Zn/Al/Zr Fibrous Catalyst that is an Improved CO₂ Hydrogenation to Methanol Catalyst. *Catal. Lett.* **2007**, *118*, 264–269. [[CrossRef](#)]
27. Dalebout, R.; Visser, N.L.; Pompe, C.E.L.; de Jong, K.P.; de Jongh, P.E. Interplay between carbon dioxide enrichment and zinc oxide promotion of copper catalysts in methanol synthesis. *J. Catal.* **2020**, *392*, 150–158. [[CrossRef](#)]
28. Lozano, L.A.; Faroldi, B.M.C.; Ulla, M.A.; Zamaro, J.M. Metal–Organic Framework-Based Sustainable Nanocatalysts for CO Oxidation. *Nanomaterials* **2020**, *10*, 165. [[CrossRef](#)]
29. Falcaro, P.; Ricco, R.; Yazdi, A.; Imaz, I.; Furukawa, S.; Maspoch, D.; Ameloot, R.; Evans, J.D.; Doonan, C.J. Application of metal and metal oxide nanoparticles@MOFs. *Coord. Chem. Rev.* **2016**, *307*, 237–254. [[CrossRef](#)]
30. Jiao, Y.; Liu, Y.; Zhu, G.; Hungerford, J.T.; Bhattacharyya, S.; Lively, R.P.; Sholl, D.S.; Walton, K.S. Heat-Treatment of Defective UiO-66 from Modulated Synthesis: Adsorption and Stability Studies. *J. Phys. Chem. C* **2017**, *121*, 23471–23479. [[CrossRef](#)]
31. Farrusseng, D.; Aguado, S.; Pinel, C. Metal–organic frameworks: Opportunities for catalysis. *Angew. Chem. Int. Ed.* **2009**, *48*, 7502–7513. [[CrossRef](#)]
32. Kobayashi, H.; Taylor, J.M.; Mitsuka, Y.; Ogiwara, N.; Yamamoto, T.; Toriyama, T.; Matsumura, S.; Kitagawa, H. Charge transfer dependence on CO₂ hydrogenation activity to methanol in Cu nanoparticles covered with metal–organic framework systems. *Chem. Sci.* **2019**, *10*, 3289–3294. [[CrossRef](#)]
33. Kang, S.-H.; Bae, J.W.; Prasad, P.S.S.; Oh, J.-H.; Jun, K.-W.; Song, S.-L.; Min, K.-S. Influence of Ga addition on the methanol synthesis activity of Cu/ZnO catalyst in the presence and absence of alumina. *J. Ind. Eng. Chem.* **2009**, *15*, 665–669. [[CrossRef](#)]
34. Mota, N.; Guil-Lopez, R.; Pawelec, B.G.; Fierro, J.L.G.; Navarro, R.M. Highly active Cu/ZnO–Al catalyst for methanol synthesis: Effect of aging on its structure and activity. *RSC Adv.* **2018**, *8*, 20619–20629. [[CrossRef](#)]
35. Arena, F.; Barbera, K.; Italiano, G.; Bonura, G.; Spadaro, L.; Frusteri, F. Synthesis, characterization and activity pattern of Cu–ZnO/ZrO₂ catalysts in the hydrogenation of carbon dioxide to methanol. *J. Catal.* **2007**, *249*, 185–194. [[CrossRef](#)]
36. Fei, J.-H.; Yang, M.-X.; Hou, Z.-Y.; Zheng, X.-M. Effect of the Addition of Manganese and Zinc on the Properties of Copper-Based Catalyst for the Synthesis of Syngas to Dimethyl Ether. *Energy Fuels* **2004**, *18*, 1584–1587. [[CrossRef](#)]
37. Wu, J.; Luo, S.; Toyir, J.; Saito, M.; Takeuchi, M.; Watanabe, T. Optimization of preparation conditions and improvement of stability of Cu/ZnO-based multicomponent catalysts for methanol synthesis from CO₂ and H₂. *Catal. Today* **1998**, *45*, 215–220. [[CrossRef](#)]

38. Ren, J.; Langmi, H.W.; North, B.C.; Mathe, M.; Bessarabov, D. Modulated synthesis of zirconium-metal organic framework (Zr-MOF) for hydrogen storage applications. *Int. J. Hydrogen Energy* **2014**, *39*, 890–895. [[CrossRef](#)]
39. Cavka, J.H.; Jakobsen, S.; Olsbye, U.; Guillou, N.; Lamberti, C.; Bordiga, S.; Lillerud, K.P. A new zirconium inorganic building brick forming metal organic frameworks with exceptional stability. *J. Am. Chem. Soc.* **2008**, *130*, 13850–13851. [[CrossRef](#)]
40. Dyosiba, X.; Ren, J.; Musyoka, N.M.; Langmi, H.W.; Mathe, M.; Onyango, M.S. Feasibility of Varied Polyethylene Terephthalate Wastes as a Linker Source in Metal–Organic Framework UiO-66(Zr) Synthesis. *Ind. Eng. Chem. Res.* **2019**, *58*, 17010–17016. [[CrossRef](#)]
41. Li, Z.; Zhao, S.; Wang, H.; Peng, Y.; Tan, Z.; Tang, B. Functional groups influence and mechanism research of UiO-66-type metal-organic frameworks for ketoprofen delivery. *Colloids Surf. B Biointerfaces* **2019**, *178*, 1–7. [[CrossRef](#)]
42. Li, C.; Yuan, X.; Fujimoto, K. Development of highly stable catalyst for methanol synthesis from carbon dioxide. *Appl. Catal. A Gen.* **2014**, *469*, 306–311. [[CrossRef](#)]
43. Vellingiri, K.; Kumar, P.; Deep, A.; Kim, K.-H. Metal-organic frameworks for the adsorption of gaseous toluene under ambient temperature and pressure. *Chem. Eng. J.* **2017**, *307*, 1116–1126. [[CrossRef](#)]
44. Valenzano, L.; Civalleri, B.; Chavan, S.; Bordiga, S.; Nilsen, M.H.; Jakobsen, S.; Lillerud, K.P.; Lamberti, C. Disclosing the Complex Structure of UiO-66 Metal Organic Framework: A Synergic Combination of Experiment and Theory. *Chem. Mater.* **2011**, *23*, 1700–1718. [[CrossRef](#)]
45. Pan, Y.; Jiang, S.; Xiong, W.; Liu, D.; Li, M.; He, B.; Fan, X.; Luo, D. Supported CuO catalysts on metal-organic framework (Cu-UiO-66) for efficient catalytic wet peroxide oxidation of 4-chlorophenol in wastewater. *Microporous Mesoporous Mater.* **2020**, *291*, 109703. [[CrossRef](#)]
46. Behrens, M. Meso- and nano-structuring of industrial Cu/ZnO/(Al₂O₃) catalysts. *J. Catal.* **2009**, *267*, 24–29. [[CrossRef](#)]
47. Peng, B.; Feng, C.; Liu, S.; Zhang, R. Synthesis of CuO catalyst derived from HKUST-1 temple for the low-temperature NH₃-SCR process. *Catal. Today* **2018**, *314*, 122–128. [[CrossRef](#)]
48. Ye, Q.; Wang, L.; Yang, R.T. Activity, propene poisoning resistance and hydrothermal stability of copper exchanged chabazite-like zeolite catalysts for SCR of NO with ammonia in comparison to Cu/ZSM-5. *Appl. Catal. A Gen.* **2012**, *427–428*, 24–34. [[CrossRef](#)]
49. Alayoglu, S.; Beaumont, S.K.; Zheng, F.; Pushkarev, V.V.; Zheng, H.; Iablokov, V.; Liu, Z.; Guo, J.; Kruse, N.; Somorjai, G.A. CO₂ hydrogenation studies on Co and CoPt bimetallic nanoparticles under reaction conditions using TEM, XPS and NEXAFS. *Top. Catal.* **2011**, *54*, 778–785. [[CrossRef](#)]
50. Zhong, L.; Chen, D.; Zafeiratos, S. A mini review of in situ near-ambient pressure XPS studies on non-noble, late transition metal catalysts. *Catal. Sci. Technol.* **2019**, *9*, 3851–3867. [[CrossRef](#)]
51. Titus, D.; James Jebaseelan Samuel, E.; Roopan, S.M. Chapter 12—Nanoparticle characterization techniques. In *Green Synthesis, Characterization and Applications of Nanoparticles*; Shukla, A.K., Irvani, S., Eds.; Elsevier: Amsterdam, The Netherlands, 2019; pp. 303–319.
52. Yang, Y.; Xu, Y.; Ding, H.; Yang, D.; Cheng, E.; Hao, Y.; Wang, H.; Hong, Y.; Su, Y.; Wang, Y.; et al. Cu/ZnOx@UiO-66 synthesized from a double solvent method as an efficient catalyst for CO₂ hydrogenation to methanol. *Catal. Sci. Technol.* **2021**, *11*, 4367–4375. [[CrossRef](#)]
53. Stangeland, K.; Kalai, D.; Li, H.; Yu, Z. CO₂ Methanation: The Effect of Catalysts and Reaction Conditions. *Energy Procedia* **2017**, *105*, 2022–2027. [[CrossRef](#)]
54. Joo, O.-S.; Jung, K.-D.; Moon, I.; Rozovskii, A.Y.; Lin, G.I.; Han, S.-H.; Uhm, S.-J. Carbon Dioxide Hydrogenation To Form Methanol via a Reverse-Water-Gas-Shift Reaction (the CAMERE Process). *Ind. Eng. Chem. Res.* **1999**, *38*, 1808–1812. [[CrossRef](#)]
55. An, B.; Zhang, J.; Cheng, K.; Ji, P.; Wang, C.; Lin, W. Confinement of Ultrasmall Cu/ZnOx Nanoparticles in Metal–Organic Frameworks for Selective Methanol Synthesis from Catalytic Hydrogenation of CO₂. *J. Am. Chem. Soc.* **2017**, *139*, 3834–3840. [[CrossRef](#)] [[PubMed](#)]
56. Portha, J.-F.; Parkhomenko, K.; Kobl, K.; Roger, A.-C.; Arab, S.; Commenge, J.-M.; Falk, L. Kinetics of Methanol Synthesis from Carbon Dioxide Hydrogenation over Copper–Zinc Oxide Catalysts. *Ind. Eng. Chem. Res.* **2017**, *56*, 13133–13145. [[CrossRef](#)]
57. Joo, S.H.; Park, J.Y.; Tsung, C.-K.; Yamada, Y.; Yang, P.; Somorjai, G.A. Thermally stable Pt/mesoporous silica core–shell nanocatalysts for high-temperature reactions. *Nat. Mater.* **2009**, *8*, 126–131. [[CrossRef](#)] [[PubMed](#)]